Hydrogenation of cinnamaldehyde to cinnamyl alcohol with metal phosphides: Catalytic consequences of product and pyridine doping

Yolanda Bonita[a,1], Varsha Jain[b,1], Feiyang Geng[a], Timothy P. O'Connell[a], Norbert X. Ramos[a], Neeraj Rai[b,*], and Jason C. Hicks[a,*]

[a]Department of Chemical and Biomolecular Engineering, University of Notre Dame, 250 Nieuwland Science Hall, Notre Dame, Indiana 46556, United States

[b] Dave C. Swalm School of Chemical Engineering and Center for Advanced Vehicular Systems, Mississippi State University, Mississippi State, Mississippi 39762, United States

---

Corresponding author email: jhicks3@nd.edu (J. C. Hicks); neerajrai@che.msstate.edu (N. Rai)

[1]These authors contribute equally to this article

Abstract

Selective hydrogenation of α,β-unsaturated aldehydes is challenging due to the competition between unsaturated functional groups (C=C and C=O) with the catalyst. This study probes the use of metal phosphides as selective catalysts for cinnamaldehyde hydrogenation. Monometallic phosphides (MP; M = Ni, Co, Ru) showed high affinity to C=C hydrogenation, with 98% selectivity to hydrocinnamaldehyde with both Ni_2P and Co_2P. Bimetallic RuMoP improved the cinnamyl alcohol (COL) selectivity up to 91%, while bimetallic NiMoP preferred C=C hydrogenation to hydrocinnamaldehyde. Density functional theory (DFT) suggested greater charge transfer between the carbonyl oxygen and Mo sites on the surface leading to a lower activation energy barrier for cinnamaldehyde hydrogenation to COL. Product and pyridine doping studies resulted in an increased selectivity to COL possibly through surface coverage effects. Lastly, diffuse reflectance infrared Fourier transform spectra and DFT provided insights into the CAL adsorption mode and the reaction mechanism that supported the experimental observation.

1. Introduction

Chemoselective hydrogenation of α,β-unsaturated carbonyl compounds obtained from biomass remains challenging due to the competition between hydrogenation of the alkene (C=C) and carbonyl (C=O) groups.[1] The hydrogenation of cinnamaldehyde (a representative α,β-unsaturated carbonyl compound) produces hydrocinnamaldehyde (HCAL) and cinnamyl alcohol (COL) for the selective hydrogenation of C=C (ΔH_{rxn} = -134 kJ/mol) and C=O (ΔH_{rxn} = -66 kJ/mol), respectively (Scheme 1). These products are important chemical intermediates in fragrances, food, and pharmaceuticals.[2] Thermodynamically, the alkene is favored, and catalysts selective to the hydrogenation of the carbonyl without reducing the C=C group are desired.

Many factors such as particle size,[2, 3] support effects,[4] solvent,[2] and alloying[5-8] are used as strategies to tune catalytic selectivity to COL. Surface modification in the form of a self-assembled monolayer (SAM) has also been reported, where functionalized thiol groups create surface constraints that force adsorption through the carbonyl group to control selectivity.[9, 10] Indeed, other studies have also shown that the C=O interaction to the catalyst surface is key to tuning the selectivity to COL,[8] and these interactions can also be enhanced through the addition of an electropositive metal.[6] For example, the selectivity to COL using a Co catalyst can be significantly improved by adding either Ga or In, where the electropositive metals served as the C=O adsorption site.[6] Similar observations have also been reported with Ru-Sn$^{\delta+}$/ ZrO_2 catalysts.[3]

A variety of monometallic phosphides, *M*P (*M* = Mo, W, Fe, Co, Ni), have been reported as effective CAL hydrogenation catalysts for the synthesis of HCAL.[11] However, the addition of a second metal to form bimetallic phosphides can drastically alter the selectivity of the catalysts.[12] In Mo-based bimetallic systems, the surface electronic structure can be altered by the addition of a second metal, which determines the adsorption orientation of the reactants on the surface.[13-

16] In the case of oxygenated substrates, the interaction between the lone pair electrons in O and the catalyst surface is essential in facilitating the C-O or C=O bond activation.[17, 18] In a recent study, bimetallic RuMoP was discovered as an active catalyst for low temperature hydrogenation reactions of aldehydes to primary alcohols with >99% selectivity.[19] The Lewis acidic nature of the RuMoP surface, originating from the partially positive charge in Mo due to charge transfer between the atoms in the RuMoP lattice, was responsible for the high alcohol selectivity.[16, 19]

Herein, the catalytic performance of RuMoP was evaluated for the liquid phase hydrogenation of CAL. Metal substitution was investigated in *M*MoP (*M* = Ru, Ni, Co) to determine if and how the selectivity can be tuned by variation in the bulk composition. For comparison, the catalytic performance of monometallic Ni, Co, Ru, and Mo phosphides were also investigated for the hydrogenation of CAL. We discovered that surface competition between the substrates and products existed, whereby the selectivity to carbonyl reduction increased with the addition of various products. By incorporating products in the feed through a recycle stream or using the product mixture as a solvent, the process would minimize the need for other reagents or leached thiol-based contaminants and could serve as a green approach to reduce waste. Infrared spectroscopy was used to observe and compare the adsorption of CAL on the different bimetallic catalysts. Lastly, the activation energy barrier for H-addition was calculated using density functional theory (DFT) to provide mechanistic insights into these transformations.

2. Methods

2.1. Materials

$(NH_4)_6Mo_7O_{24}\cdot 4H_2O$ (Alfa Aesar, 81-83% MoO_3) , $RuCl_3\cdot xH_2O$ (Oakwood, 67%), $(NH_4)_2HPO_4$ (VWR, 99%), citric acid monohydrate (VWR, 99%), $Ni(NO_3)_2\cdot 6H_2O$ (Alfa Aesar, 98%), $Co(NO_3)_2\cdot 6H_2O$ (Alfa Aesar, 98-102%), cinnamaldehyde (Milipore Sigma, 98%), 2-propanol (J.T. Baker, 99%), cinnamyl alcohol (Acros

Organics, 98%), benzenepropanol (Alfa Aesar, 99%), 3-phenylpropionaldehyde (Alfa Aesar, 99%), pyridine (EMD Milipore, 99%).

H_2 (Airgas, 99.999%), N_2 (Airgas, 99.999%), 1.01% O_2/He (Airgas), 30%CO/He (Airgas), 5%H_2/Ar (Airgas)

2.2. Catalyst synthesis

Unsupported monometallic and bimetallic phosphides were synthesized by temperature programmed reduction (TPR) as described in previous studies.[16]

To synthesize the bimetallic phosphides, 0.7 mmol of citric acid is mixed with 0.72 mmol of $(NH_4)_6Mo_7O_{24}\cdot4H_2O$, 5 mmol of $RuCl_3\cdot xH_2O$/ $Co(NO_3)_2\cdot6H_2O$/ $Co(NO_3)_2\cdot6H_2O$, and 5 mmol of $(NH_4)_2HPO_4$ in 25 mL of water. The mixture was calcined at 200°C for 2 h with 1°C/min temperature ramp. The dried mixture was ground into a fine powder. The calcination step was continued to 550°C with a 1°C/min ramp rate for 6 h. The resulting powder was reduced under 160 mL/min of H_2 at 650°C for 2 h with 5°C/min ramp rate. Lastly, the reduced powder was passivated with 160 mL/min of 1% O_2/He before it was stored in the glove box. Similarly, monometallic phosphides were synthesized with the following components: citric acid (0.7 times metal content), metal precursor (Ni: $Ni(NO_3)_2\cdot6H_2O$, Co: $Co(NO_3)_2\cdot6H_2O$, Ru: $RuCl_3\cdot xH_2O$, Mo: $(NH_4)_6Mo_7O_{24}\cdot4H_2O$), and $(NH_4)_2HPO_4$. The monometallic phosphide synthesis follows the same calcination and reduction steps as the bimetallic phosphides.

2.3. Catalyst characterization

The crystal structure of the materials was confirmed using powder XRD on a Bruker D8 Advance Davinci diffractometer. A Si (111) standard was physically mixed with the sample, and the Si (111) peak was shifted to 28.44° 2θ. The bulk composition of the material was determined using inductively coupled plasma – optical emission spectroscopy (ICP-OES; PerkinElmer Optima 8000). N_2 physisorption was used to obtain the surface area of the synthesized materials, which was collected on a Quantachrome Nova 2200e instrument. The sample was pretreated at 150°C under vacuum for at least 12 hours prior to analysis. The Brunnauer-Emmett-Teller (BET) analysis was used to calculate the surface area of the materials. The H_2 uptake for each material was quantified with H_2 TPR with a Micromeritics Chemisorb unit with a thermal conductivity detector (TCD). Approximately 50 mg of the sample was pretreated with 30 mL/min Ar flow at 850°C for 1 h with 10°C/min ramp rate. After cooling the sample to 50°C, the gas flow was switched to 30 mL/min 5% H_2 in He. Lastly, the sample was heated slowly to 850°C for 1 h with a 1°C/min ramp rate. During these steps, a trap was installed before the TCD and was cooled to 77°C to prevent water contamination in the measurements.

The nature of the surface sites was probed with pyridine adsorption via DRIFT spectra. The DRIFTS experiments were performed with a Bruker Vertex 70 with a liquid N_2 cooled mercury-cadmium-telluride (MCT). For each experiment, 80.0 mg KBr was placed in the sample cup followed by ~20.0 mg of the catalyst powder. The sample was then pressed to create a relatively flat surface. The sample was pretreated under 30 mL/min of H_2 at 400°C for 2 h. Background scans were obtained at both 100°C and 50°C under 30 mL/min of N_2 flow to appropriately examine spectra at different temperatures. Pyridine adsorption was performed at the desired temperature by flowing N_2 through a bubbler containing pyridine to contact with the catalyst surface (~ 1 h). After saturation, physisorbed pyridine on the catalyst was removed by flowing N_2 for 20 mins. A similar procedure was applied for CAL adsorption by placing CAL in the bubbler instead of pyridine.

2.4. Catalyst testing

All catalyst testing was completed in a custom made up-flow stainless steel reactor. The catalyst was pelletized to 60-100 mesh and was diluted 4 times with SiO_2 gel. Before the feed solution was introduced, the catalyst was pretreated at 400°C under 100 mL/min of H_2 flow for 1 h and subsequently cooled to the reaction temperature (125°C). After pressurizing the system to 4.2 MPa, the liquid feed was introduced with a Hitachi L-6000 HPLC pump. For the doping study, the liquid feed was switched quickly during reaction to a separate feed reservoir containing the desired amount of the dopant. Samples were collected using a sampling port and were analyzed with an Agilent 7860A gas chromatograph – 5975 mass spectrometer (GCMS). Calibration curves were made using the reactants and products to quantify the reaction progress. W/F is calculated by dividing the amount of CO titrated surface sites (N_{CO}) of catalyst loaded in the reactor by the molar flow rate of CAL in the feed (F_{CAL}).

2.5. Computational methods

DFT calculations were performed using Vienna *ab Initio* Simulation Package (VASP.5.4.4)[20,21] and employed optB88-vdW density functional.[22] Projector augmented wave (PAW)[23] approach was used to solve the Kohn-Sham equations.[20] An energy cutoff of 450 eV was used for all calculations. We found that the 450 eV cutoff is satisfactory for the convergence of the total energies, energy differences, and structural parameters. The electronic energy convergence was set at 10^{-5} eV, the same criteria were used in our previous studies.[15, 16] The convergence for forces during the structural relaxation is set at 0.03 eV/Å. Spin-polarization was included in all calculations with gamma point sampling of the Brillouin zone.[24] For the structural relaxation, the first-order Methfessel-Paxton smearing[25] was employed with a σ of 0.1 eV.

The slabs used for simulations, consist of three and four layers in RuMoP (112) and NiMoP (111), respectively, with a supercell size P (2 X 2) with a 15 Å vacuum layer in the z-direction (perpendicular to the surface) to minimize interactions between neighboring image slabs. For all calculations, the bottom most layer was fixed to represent the corresponding crystal structure obtained from DFT, whereas all other atoms were allowed to relax.

The binding energy was calculated as:

$$E_{BE} = E_{ADSORBATE+SURFACE} - E_{SURFACE} - E_{ADSORBATE} \qquad \text{(Equation 1)}$$

The binding energies (denoted as E_{BE}) were calculated according to Equation 1, wherein $E_{\mathrm{ADSORBATE+SURFACE}}$ is defined as the total energy of species adsorbed on the surface and the slab; E_{SURFACE} is defined the total energy of slab; and $E_{\mathrm{ADSORBATE}}$ is defined as the energy of the adsorbed species on the surface in the gas phase.

The activation energy barriers were defined as:

$$E_{\mathrm{A}} = E_{\mathrm{TS}} - E_{\mathrm{IS}} \qquad \text{(Equation 2)}$$

The energy barriers were obtained by taking the difference between the energy of the transition state (E_{TS}) and its corresponding initial state (E_{IS}) as shown in Equation (2). Transition states were located using the nudged elastic band (NEB) method[26] and these were further refined with the climbing image nudged elastic band (CINEB) method.[27] The identified transition states were confirmed by examining vibrational frequencies.

3. Results and discussion

3.1. Monometallic and bimetallic phosphide screening

Monometallic and bimetallic phosphides were synthesized using a temperature programmed reduction (TPR) method described in the experimental section. The H_2 uptake during reduction was quantified using a chemisorption instrument connected to a thermal conductivity detector (Table S1). The TPR profiles of post-calcined materials are plotted in Figure 1. From the Co_2P TPR profile, a smaller peak at 320°C from CoO_x was observed, while the Co phosphate reduction showed higher temperature peaks.[28] Similarly, the reduction of Ni_2P precursors yielded multiple H_2 consumption peaks. The peaks at 180°C and 430°C arise from bulk NiO_x reduction, while the peaks at 500-700°C are due to Ni phosphate reduction.[29] For Ru-based metal phosphides, low temperature peaks were observed. For example, in RuP and Ru_2P, reduction events occurred between 100°C – 400°C, which were likely from reduction of the oxidic Ru after calcination.[30, 31] MoP reduction commenced at slightly higher temperatures than other materials

(500°C) and resulted in the conversion of the MoO_x precursor to form MoP.[31, 32] The bimetallic phosphides (CoMoP, NiMoP, and RuMoP) also displayed H_2 consumption peaks at higher temperature, which were also associated with MoO_x reduction.[32] For RuMoP, the lower temperature peak at 200°C might originate from RuO_x reduction. Interestingly, the RuP, Ru_2P, and RuMoP showed different TPR profiles due to differences in the metal to P ratio and bimetallic composition.[29, 30] Overall, the TPR profiles provided reduction temperature ranges for the materials. In the case of MoP, holding the reduction temperature at 650°C for 2 h was sufficient to convert the oxidic precursor to reduced metal phosphides with defined crystal structures.[33] Therefore, the reduction step during the synthesis was conducted at 650°C for 2 h. One exception was CoMoP whose defined crystal structure was observed after reduction at 750°C, which was confirmed by the TPR profile.

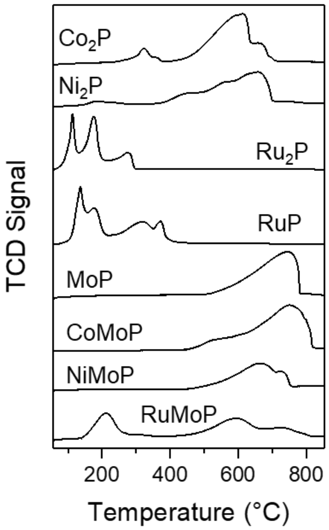

Figure 1. TPR profile of monometallic and bimetallic Co, Ni, Ru, and Mo phosphides

After reduction, the crystal structures of the various phosphides were confirmed using powder x-ray diffraction (XRD) in Figure S1 and S2, where the diffraction patterns matched the respective reference data for all monometallic and bimetallic phosphides. The bulk composition was quantified with ICP-OES to showing the composition was nearly identical to the targeted composition (Table S2). The Brunnauer-

Emmett-Teller surface area (S_{BET}) of the materials was determined with N_2 physisorption. As shown in Table S2, the surface area of the unsupported powders was in the range of 5 – 8 m^2/g, which is typical for these materials.

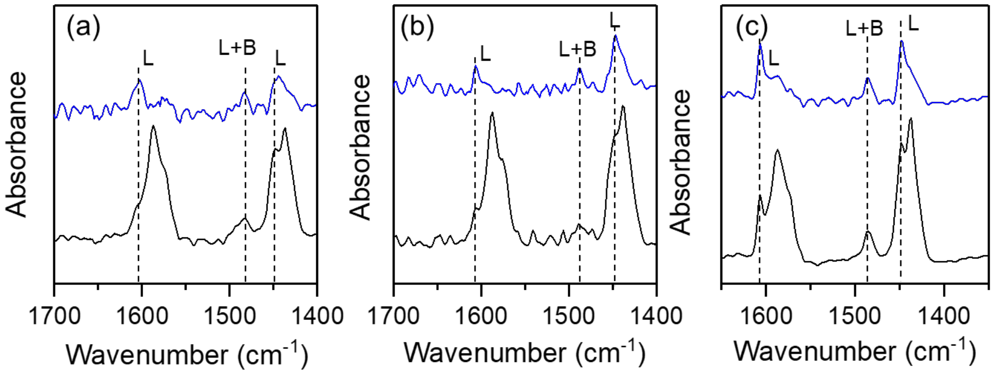

Figure 2. Pyridine adsorption on bimetallic (a) CoMoP, (b) NiMoP, and (c) RuMoP under DRIFT spectroscopy at pyridine saturation (black) and after N_2 purging (blue)

Pyridine adsorption was performed using DRIFTS to determine the nature of acid site of the materials. The pyridine adsorption modes on bimetallic CoMoP, NiMoP, and RuMoP are presented in Figure 2 a-c. For the pyridine saturated surface, features at 1590 cm^{-1} and 1430 cm^{-1} are assigned to physisorbed pyridine.[34] These features decreased in intensity upon purging with N_2. The remaining three features after flowing N_2 were assigned to chemisorbed pyridine. The features at 1604 cm^{-1} and 1448 cm^{-1} are assigned to v_{8a} and v_{19b} adsorption modes on Lewis sites (e.g., electron deficient site or partially oxidized metal).[34, 35] Meanwhile, the feature at 1485 cm^{-1} was assigned to coordinated pyridine on either or both Lewis and BrØnsted acid sites. However, the BrØnsted acid interaction with pyridine also yields a feature at 1550 cm^{-1}, which was not observed in any of the bimetallic phosphides. The same analysis was also performed on monometallic Co_2P, Ni_2P, Ru_2P, RuP, and MoP (Figure S3). These materials provided similar features as the bimetallic phosphide after pyridine adsorption. These observations agreed with previous reports using pyridine adsorption to probe the acidity of metal phosphides.[19, 35]

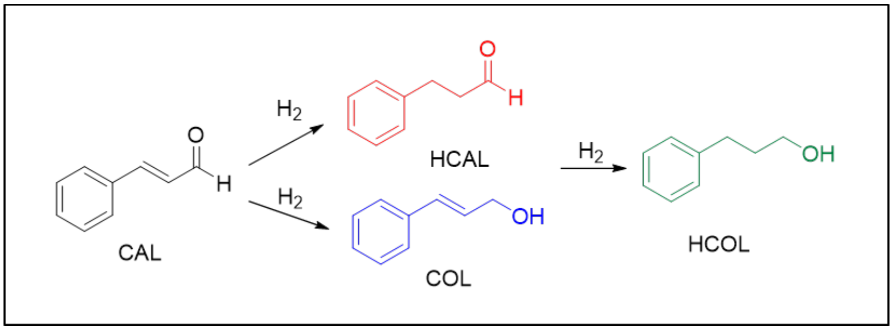

Scheme 1. Reaction pathway of CAL hydrogenation

The catalytic performance of monometallic and bimetallic phosphides was investigated for CAL hydrogenation at 125°C and 4.2 MPa. Initially, hydrogenation of CAL can occur on either the C=C group or the C=O group forming HCAL or COL, respectively (Scheme 1). The subsequent hydrogenation of HCAL and COL results in 3-phenyl-1-propanol (HCOL; Scheme 1). Although the catalytic performance of SiO_2 supported monometallic phosphides (i.e., Fe_2P, WP, MoP, CoP, Co_2P, Ni_2P, $Ni_{12}P_5$) for CAL hydrogenation has been previously investigated in other studies,[11, 36] we evaluated various monometallic phosphides to directly compare the results of all materials in this study under the same reaction conditions and conversions. The monometallic MoP, CoP, Ni_2P, RuP, and Ru_2P catalysts were tested in a flow reactor at 125°C and 4.2 MPa H_2 according to the procedure described in the experimental section. The reaction results are summarized in Table 1. First, Co_2P was tested since a previous report showed that Co_2P/SiO_2 has the highest selectivity to COL.[11] However, according to our result, Co_2P is highly selective (99-95%) to C=C bond hydrogenation to form HCAL at 5% and 20% conversion (Table 1, Entry 1 and 2). There are many possible reasons for these differences such as difference in crystal structures, elemental composition, support effects, conversion levels, and solvent. However, due to the lack of information in the structure and elemental composition from the previous study, it is challenging to determine the cause.[11] Ni_2P also showed high selectivity to HCAL (Table 1, Entry 3 and 4), which agreed with the previous report, which could possibly exclude support and solvent effects from the discrepancies seen in

Co_2P.[11] Similarly, Ru_2P provided a selectivity to HCAL of 88% at 5% conversion (Table 1, Entry 5). At a higher conversion of 75%, the selectivity to HCAL decreased to 69% while the subsequent hydrogenation to HCOL increased to 24% (Table 1, Entry 6). Meanwhile, the selectivity to COL with RuP was found to be 31% at 4% conversion (Table 1, Entry 7), which decreased to 21% at higher conversion of 27% (Table 1, Entry 8). MoP was also tested since our previous study suggested that Lewis acidic Mo is a binding site for oxygenated compounds.[14] At a conversion of 6%, the selectivity to COL was 26% (Table 1, Entry 9), which agreed with previous report.[11] However, at a higher conversion of 20%, the selectivity to COL increased significantly to 77% (Table 1, Entry 10).

Table 1. Catalytic performance of Mo, Co, Ni, and Ru monometallic phosphides at 125°C and 4.2 MPa

Entry	Catalysts	X (%)	S_{COL} (%)	S_{HCAL} (%)	S_{HCOL} (%)
1	Co_2P	5	0	99	0
2	Co_2P	20	0	95	5
3	Ni_2P	19	0	98	2
4	Ni_2P	92	1	97	2
5	Ru_2P	5	7	88	5
6	Ru_2P	75	7	68	25
7	RuP	4	31	69	0
8	RuP	27	21	75	4
9	MoP	5.8	26	73	1
10	MoP	20	77	20	3

Metal addition has been shown to alter the relative oxidation or Lewis acid character of the Mo metal studied through x-ray photoelectron spectroscopy (XPS), x-ray absorption near edge spectroscopy (XANES), and Bader charge calculation.[14-16] To improve the COL selectivity that resulted from MoP, we considered a few bimetallic Mo-based phosphides since charge transfer between the elements could improve the surface-O interaction.[3, 6] RuMoP was of interest because Ru (along with P) accepts electrons from Mo and becomes partially negative while the Mo charge is partially positive as previously shown by XPS, XANES, and Bader charge calculations (see Table S3).[16, 37] The electron transfer was initiated by the difference in electronegativity of the metals. Additionally, CoMoP and NiMoP were studied, although these materials result in less Lewis acid character for Mo.[14, 15]

The three bimetallic phosphides mentioned above (CoMoP, NiMoP, and RuMoP) were tested for CAL hydrogenation. The results are plotted in Figure S4 and Figure 3 for CoMoP, NiMoP, and RuMoP, respectively. The CoMoP catalyst (Figure S4) showed a high selectivity (99 –92%) to HCAL at conversions ranging from 3 – 30%. The NiMoP catalyst (Figure 3a) showed initial high selectivity to C=C bond hydrogenation to form HCAL. However, at longer residence times, the selectivity to HCOL increased. In comparison with the monometallic phosphides, Mo addition to Co phosphide did not produce a bimetallic effect since no improvement in selectivity was observed. Meanwhile, Mo addition to Ni phosphide increased the selectivity to HCOL, although hydrogenation of the C=C remained the dominant initial pathway. Other reports have observed increased Mo-O interactions with bimetallic NiMoP compared to monometallic Ni_2P.[38] These effects were attributed to electronic effects associated with the charge transfer from Mo to Ni and P, which lowered the electron density of Mo to become more oxophilic.[38, 39]

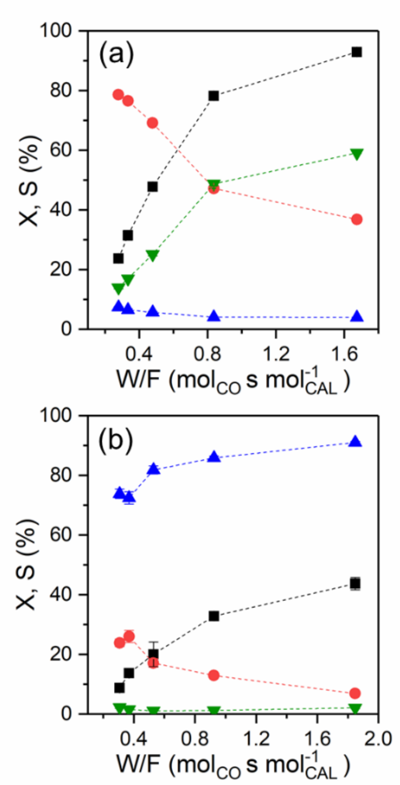

Figure 3. Conversion (X – black) and selectivity (S) of COL (blue), HCAL (red), and HCOL (green) as a function of W/F for (a) NiMoP and (b) RuMoP.

RuMoP showed a different selectivity compared to the other two catalysts. At the lowest residence time, the selectivity was 74% to COL, 24% to HCAL, and 2% to HCOL (Figure 3b). As the reaction progressed, the selectivity towards COL increased to 91% at 43% conversion. The differences in C=C and C=O hydrogenation preferences were probed further with DFT calculations for RuMoP and NiMoP. The binding configurations of the reactant (CAL) and products (COL, HCAL, and HCOL) on RuMoP and NiMoP surfaces are shown in Figure 4. CAL binding on both RuMoP and NiMoP surfaces is favorable, evident by their binding energy of -2.24 eV and -2.02 eV, respectively. However, CAL binds in a different orientation on RuMoP and NiMoP surfaces. The binding modes of CAL on RuMoP and NiMoP were deciphered through the partial atomic charges (Table S5 and S6) and distances (Table S7) post CAL binding. These results indicated that the distance of the carbonyl O atom referred to as O_1 in RuMoP (Figure S5) is closer to the surface (1.94 Å) compared to NiMoP (3.85 Å). Moreover, the charge transfer between the O_1 atom and the surface is 0.35 and 0.25 |e| for RuMoP and NiMoP respectively, which indicates higher charge transfer from the O_1 atom to the RuMoP surface. Simultaneously, the average partial charge on the neighboring Mo atoms of O_1 changes from +0.71 to +0.50 |e| and +0.65 to +0.53 |e| on RuMoP and NiMoP, respectively. This indicates that electrons are transferred from O_1 to the neighboring $Mo^{\delta+}$ sites on the RuMoP and NiMoP surface. Meanwhile, the atomic charge transfer of the carbonyl C (C_1) and α-C (C_2) in Figure S5 were very similar and within 0.03 |e|. However, the change in the partial atomic charge of the β-C (C_3) is higher in NiMoP (0.37 |e|) compared to RuMoP (0.11 |e|). The neighboring $Mo^{\delta+}$ atoms to the C_3 atom show charge difference from +0.71 to +0.65 |e| and +0.65 to +0.53 |e| over RuMoP and NiMoP, respectively. This indicates that there is higher charge transfer from C_3 atom to the NiMoP surface than RuMoP. Further, the distance of the C_3 atom to the surface is smaller in NiMoP (2.51 Å) than the RuMoP (2.84 Å) surface. This suggests that charge transfer occurs more favorably to the O_1 atom on RuMoP and C_3 atom on NiMoP, which might account for the C=O and C=C selectivity, respectively.

NiMoP showed the selectivity shifts from HCAL to HCOL at longer W/F values (Figure 3a) indicating further saturation of the C=O bond in HCAL. Indeed, DFT calculations suggest there is charge transfer to the C_1 and O_1 atoms evident by the charge transfers of 0.13 |e| and 0.11 |e|, respectively in HCAL over NiMoP. The average partial charge in the neighboring $Mo^{\delta+}$ atoms of C_1 and O_1 atoms changes from +0.65 to +0.59 |e| and +0.61 |e|, respectively over NiMoP. This observation is the opposite of RuMoP where the partial atomic charge is smaller on C_1 (0.09 |e|) and O_1 (0.07 |e|) in HCAL. Furthermore, partial charge on the neighboring $Mo^{\delta+}$ atoms changes from +0.71 to +0.67 |e| and +0.68 |e| for C_1 and O_1 atoms, respectively on the RuMoP surface. These results showed that the change in charges of C_1 and O_1 atoms is because of the tendency of $Mo^{\delta+}$ atoms to gain electrons. Additionally, change in the partial atomic charge of C_2 (0.03 |e|) and C_3 (0.09 |e|) atoms in COL on the RuMoP surface is small in comparison to NiMoP (0.08 and 0.19|e| for C_2 and C_3, respectively). The lack of charge transfer from atoms of RuMoP surface to COL and HCAL account for the high COL selectivity with minimal subsequent hydrogenation in RuMoP.

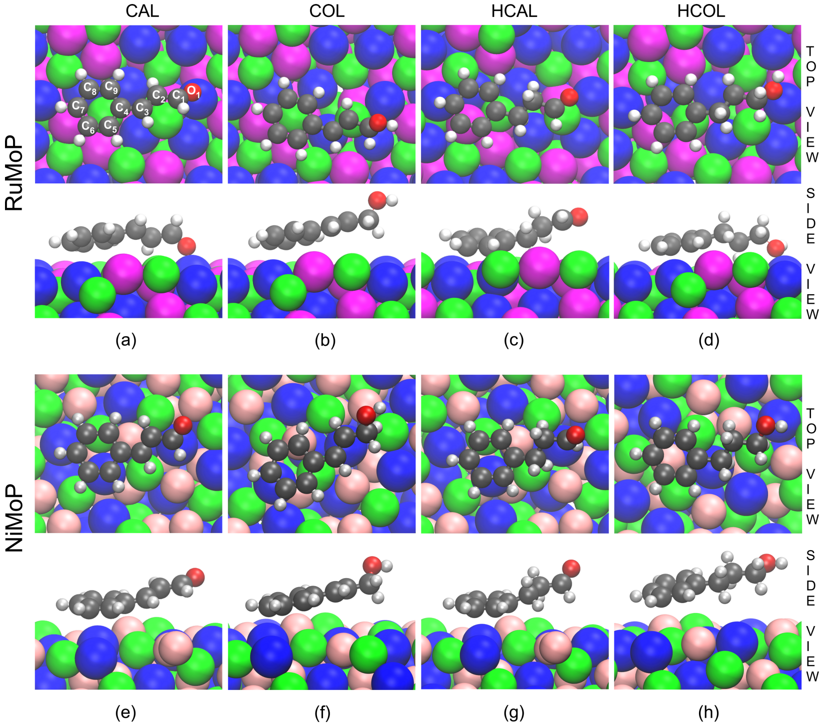

Figure 4. Optimized structures of CAL, COL, HCAL, and HCOL on RuMoP (112) (a-d) and NiMoP (111) (e-h) (purple for Ru; pink for Ni; blue for Mo; green for P; grey for C; silver for H; red for O).

At longer residence times with NiMoP, the hydrogenation of the unconjugated C=O bond becomes favorable (HCOL favored). However, an interesting trend was observed with RuMoP at longer residence times, where hydrogenation of the conjugated C=O becomes more favorable (COL favored). This result could imply that surface effects associated with surface crowding of reactive intermediates and products influence the selectivity. Therefore, further experiments were performed to study the effect of dopants on the COL selectivity.

3.2. Modulation study with dopants

Various dopants were investigated to modulate the catalyst selectivity by switching the feed stream to one containing a different composition of reactive species. Prior to the modulation study, the following experiments were performed to determine independent interactions between HCAL and COL on the RuMoP surface (Figure S6). First, 0.10 M of CAL was used as the feed to establish a conversion baseline. After the feed was switched to 0.10 M HCAL, ~28% HCAL was converted to HCOL, showing that HCAL would react over RuMoP to form HCOL . The feed was switched again to CAL to ensure the stability of the catalyst at which the original conversion was recovered. Next, COL was fed to the reactor, and an average of 2.1% of the COL was converted to HCOL. From this experiment, we hypothesized that COL might interact with the RuMoP surface but that it was not significantly reactive. CAL was subsequently fed into the reactor to establish steady-state conversion of CAL and showcase the stability of the catalyst. Lastly, the concentration of CAL was increased, and the conversion levels remained stable.

The first modulation experiment was performed with COL as a dopant since it is the most dominant product observed during the reaction of CAL with RuMoP (Figure 5a). The experiment began with a fresh feed of CAL to establish an initial steady state baseline to observe any noticeable effects from the additives. After steady state was achieved at 8% conversion and 76% selectivity to COL, the feed was switched to 95%:5% CAL:COL while keeping the total concentration at 0.10 M. Because COL is also a product, the added amount was assumed unreactive. Therefore, the difference between the final COL amount in the outlet and the COL in the initial feed was attributed to the produced COL. The assumption that COL is unreactive is verified from experiments using it as a feed, which showed less than 2% COL converted under similar conditions. With COL in the feed, the selectivity to COL increased to ~90%. When the COL concentration was increased to 25% or 50%, the selectivity to COL remained at 91%. At 50% COL concentration, the conversion slightly increased due to the lower content of CAL in the feed. At the end of the experiment, the feed was switched back to the original CAL composition without added dopant, and both selectivity and conversion were recovered to the steady state value (Figure 5a). The results suggested that COL interacts with the surface to modulate the selectivity of CAL to COL, which is likely the reason the COL selectivity increased over RuMoP as a function of W/F.

The same doping experiment was performed with NiMoP. It could be seen that the selectivity to COL increased as the concentration of COL dopant in the feed was increased. At a 50:50 CAL:COL ratio, the selectivity of COL was increased to 28% compared to when no COL dopant was added (11%). However, adding COL could not increase the selectivity of COL significantly on NiMoP to match that of RuMoP. Two possible explanations of the results were (1) the high COL selectivity on RuMoP originated from the surface properties (i.e., electronics) rather than solely from surface competition effects or (2) the possibility of competition with other surface species such as HCOL and COL.

A similar study was conducted using HCOL as a dopant rather than COL on RuMoP and NiMoP (Figure 6). The same assumption was made that the differences in HCOL between the inlet and outlet is due to HCOL formation during reaction. Since the yield to HCOL is lower than COL with RuMoP, the doping experiment was performed with a lower HCOL:CAL ratio. At 99.5:0.5 CAL:HCOL, the selectivity to COL increased to 91% COL, showing that HCOL also aided in the production of COL. The HCOL amount was increased up to CAL:HCOL of 98:2, but the selectivity remained at ~91% COL. Finally, the initial selectivity was recovered when the feed was switched to CAL without HCOL dopant.

HCOL doping was also performed on NiMoP catalyst to determine if the doping technique can be used to tune the selectivity in NiMoP. At CAL:HCOL of 95:5, the COL selectivity increased from 9% to 30%. However, the selectivity could not be significantly improved even at 50:50 CAL:HCOL feed ratio. These results show that the products could influence the COL selectivity, but the catalyst composition (i.e., RuMoP) was essential in achieving > 90% COL selectivity.

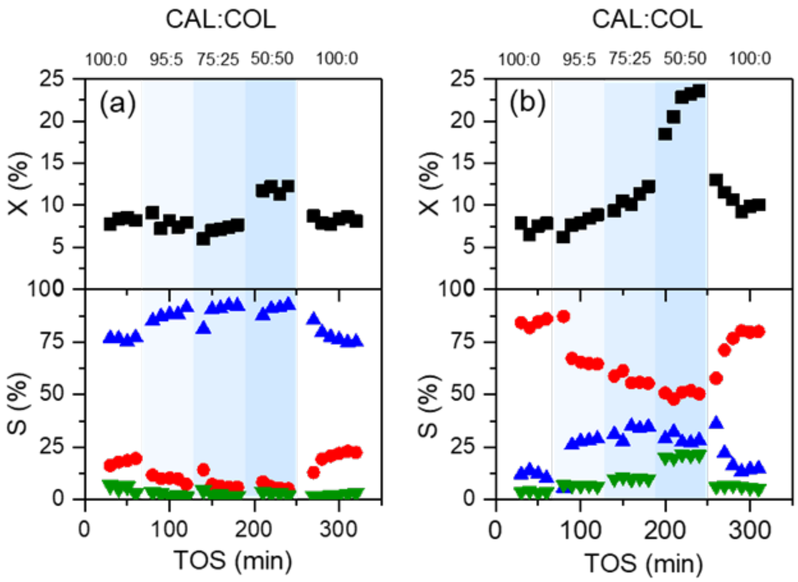

Figure 5. COL doping experiments with (a) RuMoP and (b) NiMoP and the effects on selectivity to COL (blue), HCAL (red), and HCOL (green). Temperature: 125°C, Pressure: 4.2MPa, Total concentration: 0.10 M, Flowrate: 1.0 mL/min.

The hypothetical surface interactions possible between CAL, COL, and HCOL are depicted in Scheme 2a, where π - π stacking of the adsorbed molecules may occur with excess COL or HCOL, forcing CAL to bind through the carbonyl O on RuMoP. In this configuration, the π-π stacking may stabilize the C=O adsorption on the catalyst surface. This concept is similar to the effects observed with SAMs as mentioned above where functionalized thiols are used to create sterics on the surface to force C=O adsorption similar to our observation.[10] Similar concepts have also been tested on Ni_2P functionalized with p-fluorothiols, where the p-fluorothiol functionalized Ni_2P showed an increase to COL production to almost 100%.[40] The increase in selectivity to COL was attributed to downshift in the d-band center after p-fluorothiol functionalization that increased H_2 adsorption and prevented the C=C bond from adsorbing on the active sites.[40] Although the SAM concept has been shown to improve the C=O adsorption, these methods required the use of thiol-containing components that could potentially leach to the outlet steam. However, here we show that the products alone in combination with RuMoP can modulate the reactivity and increase selectivity to COL if a recycle stream was incorporated in the reactor design. It is important to note that the COL selectivity in RuMoP was achieved through a combination of product modulation and surface electronics, as will be discussed in the following section.

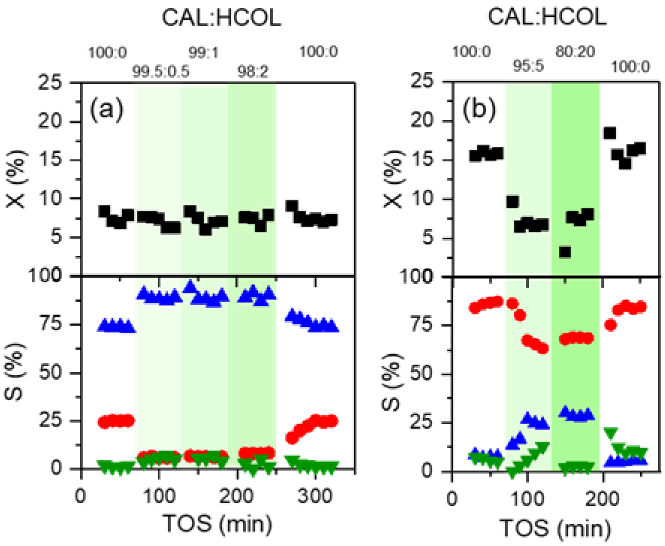

Figure 6. Conversion (black) and selectivity to COL (blue), HCAL (red), and HCOL (green) for HCOL doping on (a) RuMoP and (b) NiMoP. Temperature: 125°C, Pressure: 4.2MPa, Total concentration: 0.10 M, Flowrate: 1.0 mL/min.

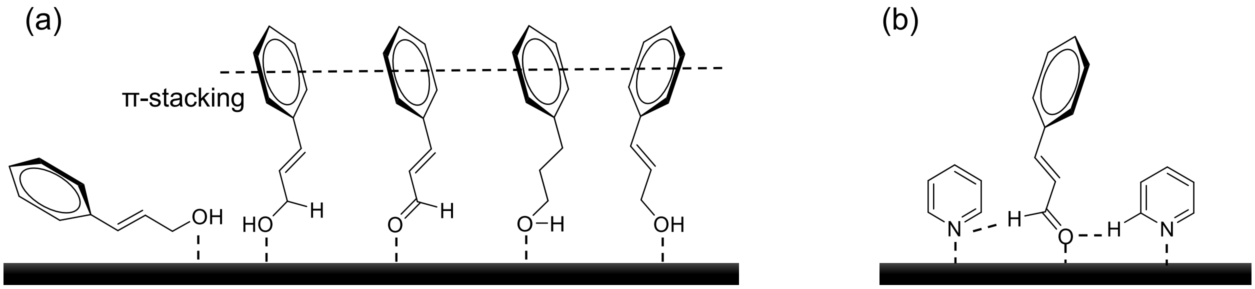

Scheme 2. (a) Possible stacking interactions between CAL, COL, and HCOL on the RuMoP and NiMoP surface and (b) possible surface interactions with both CAL and pyridine.[41]

A poisoning experiment was performed with pyridine since it has been shown to stabilize CAL adsorption through the carbonyl O on a Pd/C surface by forming a H-bond with the α-H on pyridine

(Scheme 2b).[41] The poisoning experiment was also performed on both RuMoP (Figure 7a) and NiMoP (Figure 7b). As noted previously in Figure 2, pyridine adsorption on these catalysts occurs predominantly through Lewis acidic sites, and the addition of pyridine to the reaction feed could block these sites. The experiment was initially started with a fresh, pretreated catalyst and CAL with no pyridine to obtain steady state. As expected for RuMoP, the selectivity was predominantly COL with conversion of ~6%. Upon 0.01 M pyridine doping, the conversion decreased to ~4% likely due to site blocking by pyridine, which implied that the hydrogenation site is acid site. The surface interaction with pyridine could also be observed from the increase in selectivity of COL to ~92% from ~78%, which indicates possible C=O adsorption stabilization through H-bond formation as illustrated in Scheme 2b.[41] The conversion could not be recovered to its initial value after pyridine is removed, which is due to a strong interaction between pyridine and RuMoP due to stronger Lewis acid character for this catalyst.[14] For NiMoP, the COL selectivity starts at ~10% with no pyridine at a ~21% conversion. When 0.01 M pyridine was added, a slight decrease in conversion from an average of 21% to 17% was observed, and the selectivity to COL also increased to 40%. The pyridine concentration was further increased to 0.05 M. At this point, the CAL conversion dropped drastically to an average of 4% accompanied by an increase in COL selectivity to 50%. Lastly after the feed was switch to CAL with no pyridine, the conversion could be recovered to average of 22%. Interestingly, the selectivity to HCAL increased to 97% from the original 81%. This increase is mainly from the decrease in COL formation rather than increase of HCAL formation. Additionally, some pyridine could not be removed from the surface after being flushed for 60 mins, and the leftover pyridine potentially blocked sites selective to COL.

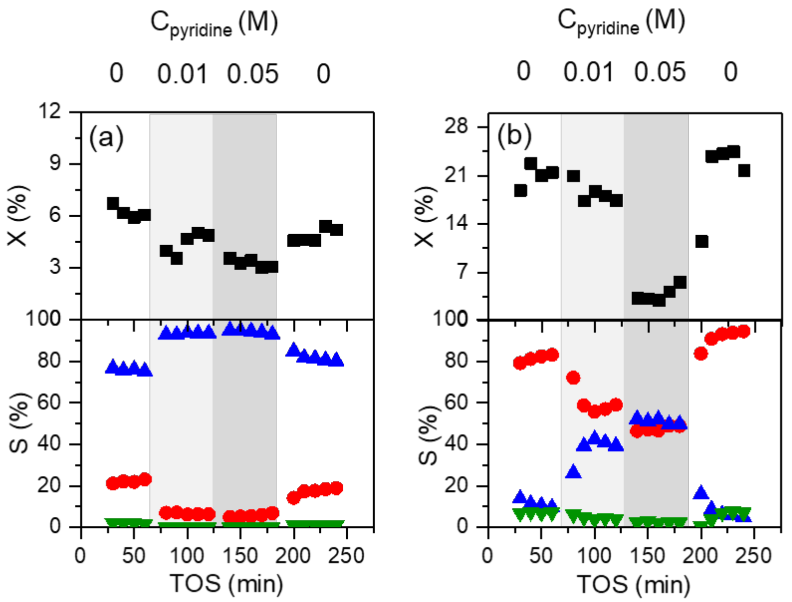

Figure 7. Conversion (black) and selectivity to COL (blue), HCAL (red), and HCOL (green) for pyridine doping during 0.10 M CAL hydrogenation on (a) RuMoP and (b) NiMoP with pyridine.

3.3. CAL surface interaction

The surface interaction between CAL and the different catalysts was studied with DRIFTS under an inert atmosphere (N_2) and under a reactive gas environment (H_2). The experiments were performed according to the procedural steps described in section 2.3 with a H_2 pretreatment step followed by substrate saturation through a N_2 bubbler and N_2 purging to remove physisorbed substrates. The spectra for the adsorption of CAL on RuMoP under N_2 after the removal of physisorbed CAL are plotted in Figure 8a. Two distinct peaks at 1680 cm^{-1} and 1624 cm^{-1} are assigned to the ν(C=O) and ν(C=C) vibrations.[6, 41, 42] The peak locations were red-shifted from the gas phase values suggesting interaction between CAL and the catalyst surface.[42] The flow of N_2 was switched to H_2 flow to observe the change in C=O and C=C surface interactions under H_2 flow. The spectrum was taken at 50°C instead of the reaction temperature 125°C to decrease the rate at which the peak disappeared. After H_2 was introduced into the cell, spectra were obtained every 2000 s. The spectra collected over time showed a reduction in the C=O peak suggesting C=O hydrogenation under H_2 flow and supporting the experimental observation of COL formation.

CAL adsorption was also performed on NiMoP (Figure 8b). The adsorption of CAL on NiMoP (black curve) generated more IR features compared to RuMoP. The C=C bond feature in NiMoP was observed at similar location as in RuMoP at 1626 cm^{-1}. However, two C=O features were observed at 1690 cm^{-1} and 1672 cm^{-1}.[42] The assignment of these C=O features are difficult due to the many proposed binding configuration of C=O such as η_1(O), η_2(C-O), π-bonded (C=O), acyl-type adsorption, and 1,4-diadsorbed species (Figure S6).[43] The η_1(O) configuration adsorbs on the catalyst surface through the O atom that leads to the C=O bond hydrogenation.[43] This is likely the configuration that is observed on RuMoP since C=O bond hydrogenation to form COL is the dominant product. In NiMoP, C=C bond hydrogenation to form HCAL is the main product. Therefore, configurations other than η_1(O) exists on NiMoP. Since C-O bond cleavage is not observed in this work, the η_2(C-O) and acyl- type adsorption modes may not be significant.[44, 45]

Similar to the RuMoP experimental setup, H_2 was flowed into the system and spectra were collected every 2000 s (Figure 8b). The C=C feature was shown to decrease over reaction time due to hydrogenation of the C=C bond. The C=O feature at 1690 cm^{-1} decreases slightly, but the C=O feature at 1672 cm^{-1} decreased at a higher rate. Since the π-bonded (C=O) is resistant to reaction with H_2 and has been observed to yield IR features near the η_1(O) features about 50 cm^{-1} upshifted similarly to adsorption on NiMoP, it is possible the feature at 1690 cm^{-1} is π-bonded (C=O).[46] This decrease in the C=O peak at 1672 cm^{-1} was possibly due to loss in conjugation after the C=C bond was hydrogenated followed by product desorption.[42] The last possible C=O adsorption is through the 1,4-diadsorbed mode as has been proposed through theory.[47] In this mode of adsorption, the O_1 and C_3 both adsorb on the catalyst surface either on one or two active sites (Figure S7), which lead to virtually no C=O bond hydrogenation.[47] Considering the partial atomic charge result for CAL adsorption (Table S6), the charge transfer from the NiMoP catalyst surface is the highest on both O_1 and C_3 position (0.25 and 0.37 |e|), which could imply that CAL adsorbed through the O_1 and C_3 position in the 1,4-diadsorbed mode.

Co-adsorption of CAL and HCOL experiments were performed on RuMoP using IR spectroscopy (Figure S8). HCOL adsorption on RuMoP under H_2 flow resulted in the spectrum shown in Figure S8. Features from HCOL were observed at 1600 cm^{-1}, 1588 cm^{-1}, 1495 cm^{-1}, and 1455 cm^{-1} representing the phenyl ring $\nu(C=C)$, $\delta(CH_3)$, and $\delta(OH)$, respectively.[48] Subsequently, CAL was introduced into the system, and the original features from HCOL could remained, but they shifted slightly to lower wavenumbers. New features from the C=C (1626 cm^{-1}) and C=O (1667 cm^{-1}) bond in CAL were also observed. The spectra showed that CAL and HCOL co-adsorbed on the RuMoP surface, which agreed with our experimental observations.

Nevertheless, the DRIFT spectra provided evidence of the $\eta_1(O)$ adsorption mode in RuMoP is essential for the hydrogenation of C=O bond. DFT calculations also confirmed that the charge transfer from the RuMoP surface is primarily through the O_1 atom. In contrast, $\eta_1(O)$ adsorption mode is not the predominant adsorption mode in NiMoP with potential π-bonded C=O or the 1,4 diadsorbed mode contributing to the hydrogenation of C=C bond.

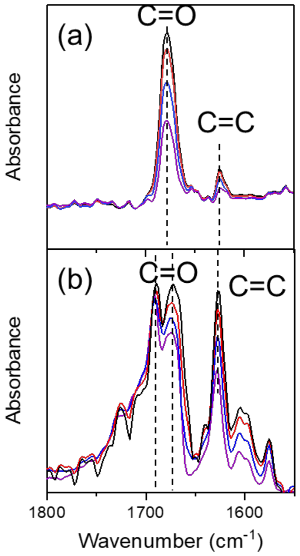

Figure 8. Cinnamaldehyde adsorption on (a) RuMoP and (b) NiMoP at saturation (black) in N_2 flow followed by H_2 flow for 2000 s (red), 4000 s (blue), and 6000 s (purple).

3.4. Computational results

DFT was performed to gain insights into CAL hydrogenation on RuMoP and NiMoP. The DFT calculation showed the first hydrogenation step of C=O on RuMoP and C=C on NiMoP in the presence of surface adsorbed hydrogens were preferential. There are 4 possible atom locations for the first H-addition: (1) O_1 or (2) C_1 for the hydrogenation of C=O bond and (3) C_2, or (4) C_3 for the hydrogenation of C=C bond as shown in Figure S9 with atom numbering shown in Figure S5. The activation energy (E_A) was calculated for the first and second H-addition on position 1 to 4 and the H-addition as described in Figure 9a and b for RuMoP and NiMoP, respectively. Pathway I and II denote the H-addition on O_1 followed by C_1 and C_1 followed by O_1, respectively. Both pathways, I and II, yield COL as the final product. Pathway III showed H-addition on C_2 followed by C_3, while pathway IV started with H-addition on C_3 followed by C_2, leading to HCAL formation (Figure S9). These hydrogenation reactions start in the presence of surface adsorbed hydrogen atoms, and the most stable binding site is determined as on the top of Mo as discussed in our past studies.[15, 19]

The transition state energy of each elementary step for the proposed reaction pathway I-IV was calculated on RuMoP(112) and NiMoP(111) as the most dominant facet seen in XRD. Pathway I and II are initiated by binding of CAL in the presence of two surface adsorbed H-atoms as shown in Figure S8a and f, respectively. This step leads to the formation of $(C_6H_5)C_2H_2CHOH^*$ and $(C_6H_5)C_2H_2CH_2O^*$ (INT1) due to the addition of one H to the O_1 and C_1 atom as shown in Figure S8c and h with the E_{BE} = -2.03 and -1.93 eV (See Figure 9a) for pathway I and II, respectively. The transition state (TS1) for this step is shown in Figure S8b and g with the E_A of 0.35 and 0.70 eV for pathway I and II, respectively. This result indicates that pathway I (H-addition on O_1) is more favorable on RuMoP, possibly due to the close proximity of O_1 on RuMoP surface as well as higher charge transfer to O_1 from the catalyst surface as mentioned in the previous section. The formed intermediate is further hydrogenated to COL ($(C_6H_5)C_2H_2CH_2OH^*$) as shown in Figure S8e and j, and the transition state (TS2) related to the second hydrogenation step is shown in Figure S8d and i for pathway I and II, respectively. The E_A for TS2 for pathway I and II are 0.68 and 0.65 eV, respectively.

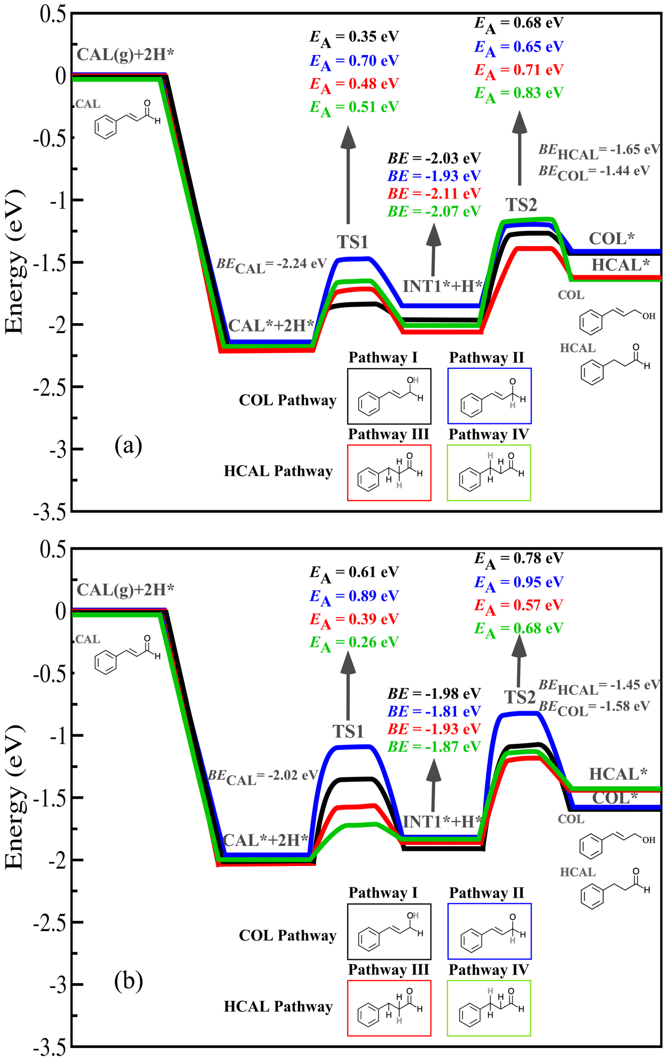

Figure 9. (a) Reaction energetics on CAL hydrogenation RuMoP(112) and (b) NiMoP(111) through pathway I-IV. The black, blue, green, and red colors represent COL pathway (I), COL pathway (II), HCAL pathway (III), and HCAL pathway (IV), respectively.

Pathway III and IV (Figure S10) were also evaluated on RuMoP(112) for the formation of $(C_6H_5)CHCH_2CHO^*$ and $(C_6H_5)CH_2CHCHO^*$ intermediate at TS1, respectively as shown in Figure S10m and r. The binding energy for these steps are -2.11 and -2.07 eV. Furthermore, this intermediate undergoes another hydrogenation step in the presence of second surface adsorbed H atom. This leads to the final product formation (HCAL) as shown in Figure S10. The TS2 related to this step has been shown in Figure S10n and s for pathway III and IV, respectively. The E_A for TS1 of pathway III and IV on RuMoP(112) are 0.48 and 0.51 eV, while the E_A for TS2 are 0.71 and 0.83 eV. The lowest E_A for TS1 and overall E_A was still through pathway I, which suggested that the first H-addition in RuMoP was more favorable through the C=O bond as evident by the high COL formation seen experimentally.

Similarly, the same analysis on the E_A of TS1 and TS2 for pathway I to IV were performed on NiMoP(111) (Figure S11). The E_A of the first H-addition step or TS1 for pathway I, II, III, and IV were 0.61, 0.89, 0.39, and 0.26 eV (See Figure 11b). The lowest E_A for the first H-addition in pathway IV implied that the most favorable H-addition was on the C_3 position > C_2 > O_1 > C_1. The E_A for TS2 for pathway I, II, III, and IV were 0.78, 0.95, 0.57, and 0.68 eV, respectively. Although the first H-addition was favorable through pathway IV, second H-addition was preferable to pathway III. Overall, pathway III and IV compete for C=C bond hydrogenation to form HCAL due to the lower E_A over NiMoP, which agreed with the experimental observation.

4. Conclusion

The selectivity of C=O and C=C bond hydrogenation in CAL was tuned with monometallic and bimetallic phosphides. Monometallic phosphides such as Ni_2P, Co_2P, RuP, Ru_2P were highly selective towards C=C bond hydrogenation with 99% selectivity achieved with Ni_2P and Co_2P catalysts. Monometallic MoP showed C=C hydrogenation preference at low conversion, but the selectivity shifted to C=O hydrogenation at higher conversion. Bimetallic RuMoP was identified as a highly selective catalyst for C=O hydrogenation (~ 91%) in contrast with other bimetallic such as NiMoP and CoMoP. Modulation studies were conducted with the products (COL and HCOL) to increase the selectivity of C=O hydrogenation in RuMoP, due to surface competition between the products (HCOL and COL) and possible π-π stacking that stabilized CAL adsorption through C=O. DRIFTS experiments of CAL adsorption showed the presence of $\eta_1(O)$ adsorption mode in RuMoP that leads to the hydrogenation of C=O bond, while NiMoP showed $\eta_1(O)$ adsorption mode and potential π-bonded C=O or 1,4-diadsorbed species that inhibited the hydrogenation of C=O bond.

Lastly, DFT calculations indicated that H_2 addition is more favorable on the C=O functionality with RuMoP. Specifically, the first H-addition was more favorable on the O_1 atom. The surface electronic structure of RuMoP greatly influenced the proximity of O_1 during adsorption. In contrast, the H-addition is more favorable on the C_3 atom with the NiMoP catalyst, making the hydrogenation of the C=C bond more favorable.

Acknowledgements

This work was supported in part by funding from the National Science Foundation through the CAREER award program (CBET-1351609 and CBET-1752036), Defense University Research Instrumentation Program under AFOSR Award No. FA9550-17-1-0376, and Center of Environmental Science and Technology (CEST) Fellowship. We thank CEST for the use ICP-OES and Material Characterization Facility (MCF) at the University of Notre Dame for the use of XRD. The computation portion of this work used resources of the High Performance Computing Collaboratory at the Mississippi State University and the National Energy Research Scientific Computing Center (NERSC). Also, computational research is supported by U.S. Department of Energy Office under Contract No. DE-AC02-05CH11231. We acknowledge VESTA[49], CANVAS, and VMD[50] for use of their software to create images of the crystal structures contained in this manuscript.

References

[1] L. Wu, T. Moteki, Amit A. Gokhale, David W. Flaherty, F.D. Toste, Production of fuels and chemicals from biomass: Condensation reactions and beyond, Chem, 1 (2016) 32-58.
[2] P. Gallezot, D. Richard, Selective Hydrogenation of α,β-Unsaturated Aldehydes, Catal. Rev., 40 (1998) 81-126.
[3] B. Coq, P.S. Kumbhar, C. Moreau, P. Moreau, M.G. Warawdekar, Liquid-phase hydrogenation of cinnamaldehyde over supported ruthenium catalysts - influence of particle-size, bimetallics and nature of support, Journal of Molecular Catalysis, 85 (1993) 215-228.

[4] A.B. da Silva, E. Jordão, M.J. Mendes, P. Fouilloux, Effect of metal-support interaction during selective hydrogenation of cinnamaldehyde to cinnamyl alcohol on platinum based bimetallic catalysts, Appl. Catal. A, 148 (1997) 253-264.
[5] S. Cattaneo, S.J. Freakley, D.J. Morgan, M. Sankar, N. Dimitratos, G.J. Hutchings, Cinnamaldehyde hydrogenation using Au–Pd catalysts prepared by sol immobilisation, Catal. Sci. Technol., 8 (2018) 1677-1685.
[6] Y.S. Yang, D.M. Rao, Y.D. Chen, S.Y. Dong, B. Wang, X. Zhang, M. Wei, Selective hydrogenation of cinnamaldehyde over Co-based intermetallic compounds derived from layered double hydroxides, ACS Catal., 8 (2018) 11749-11760.
[7] C.S. Narasimhan, V.M. Deshpande, K. Ramnarayan, Selective hydrogenation of α,β-unsaturated aldehydes to unsaturated alcohols over mixed ruthenium–tin boride catalysts, Journal of the Chemical Society, Chemical Communications, (1988) 99-100.
[8] Y.Z. Chen, S.W. Wei, K.J. Wu, Effect of promoter on selective hydrogenation of α,β-unsaturated aldehydes over cobalt borides, Appl. Catal. A, 99 (1993) 85-96.
[9] S.H. Pang, C.A. Schoenbaum, D.K. Schwartz, J.W. Medlin, Directing reaction pathways by catalyst active-site selection using self- assembled monolayers, Nat. Commun., 4 (2013).
[10] C.A. Schoenbaum, D.K. Schwartz, J.W. Medlin, Controlling the Surface Environment of Heterogeneous Catalysts Using Self-Assembled Monolayers, Accounts Chem. Res., 47 (2014) 1438-1445.
[11] H. Wang, Y.Y. Shu, M.Y. Zheng, T. Zhang, Selective hydrogenation of cinnamaldehyde to hydrocinnamaldehyde over SiO(2) supported nickel phosphide catalysts, Catalysis Letters, 124 (2008) 219-225.
[12] D.J. Rensel, S. Rouvimov, M.E. Gin, J.C. Hicks, Highly selective bimetallic FeMoP catalyst for C-O bond cleavage of aryl ethers, J. Catal., 305 (2013) 256-263.
[13] D.J. Rensel, J. Kim, V. Jain, Y. Bonita, N. Rai, J.C. Hicks, Composition-directed $Fe_xMo_{2-x}P$ bimetallic catalysts for hydrodeoxygenation reactions, Catal. Sci. Technol., 7 (2017) 1857-1867.
[14] Y. Bonita, J.C. Hicks, Periodic trends from metal substitution in bimetallic Mo-based phosphides for hydrodeoxygenation and hydrogenation reactions, J. Phys. Chem. C, 122 (2018) 13322-13332.
[15] V. Jain, Y. Bonita, A. Brown, A. Taconi, J.C. Hicks, N. Rai, Mechanistic insights into hydrodeoxygenation of phenol on bimetallic phosphide catalysts, Catal. Sci. Technol., 8 (2018) 4083-4096.
[16] Y. Bonita, V. Jain, F. Geng, T.P. O'Connell, W.N. Wilson, N. Rai, J.C. Hicks, Direct synthesis of furfuryl alcohol from furfural: catalytic performance of monometallic and bimetallic Mo and Ru phosphides, Catal. Sci. Technol., 9 (2019) 3656-3668.
[17] A.N.K. Lup, F. Abnisa, W.M.A.W. Daud, M.K. Aroua, Acidity, oxophilicity and hydrogen sticking probability of supported metal catalysts for hydrodeoxygenation process, IOP Conference Series: Materials Science and Engineering, 334 (2018) 012074.
[18] C.A. Teles, P.M. de Souza, A.H. Braga, R.C. Rabelo-Neto, A. Teran, G. Jacobs, D.E. Resasco, F.B. Noronha, The role of defect sites and oxophilicity of the support on the phenol hydrodeoxygenation reaction, Appl. Catal. B, 249 (2019) 292-305.
[19] Y. Bonita, T.P. O’Connell, H.E. Miller, J.C. Hicks, Revealing the hydrogenation performance of RuMo phosphide for chemoselective reduction of functionalized aromatic hydrocarbons, Ind. Eng. Chem. Res., 58 (2019) 3650-3658.
[20] A.D. Becke, Perspective: Fifty years of density-functional theory in chemical physics, J. Chem. Phys., 140 (2014).

[21] G. Kresse, J. Furthmüller, Efficient iterative schemes for ab initio total-energy calculations using a plane-wave basis set, Phys. Rev. B, 54 (1996) 11169-11186.
[22] J. Klimeš, D.R. Bowler, A. Michaelides, Chemical accuracy for the van der Waals density functional, J. Phys. Condens. Matter, 22 (2009) 022201.
[23] P.E. Blöchl, Projector augmented-wave method, Phys. Rev. B, 50 (1994) 17953-17979.
[24] A. Genova, M. Pavanello, Exploiting the locality of periodic subsystem density-functional theory: efficient sampling of the Brillouin zone, J. Phys. Condens. Matter, 27 (2015).
[25] M. Methfessel, A.T. Paxton, High-precision sampling for Brillouin-zone integration in metals, Phys. Rev. B, 40 (1989) 3616-3621.
[26] G. Henkelman, H. Jónsson, Improved tangent estimate in the nudged elastic band method for finding minimum energy paths and saddle points, J. Chem. Phys., 113 (2000) 9978-9985.
[27] G. Henkelman, B.P. Uberuaga, H. Jónsson, A climbing image nudged elastic band method for finding saddle points and minimum energy paths, J. Chem. Phys., 113 (2000) 9901-9904.
[28] X.Q. Wang, P. Clark, S.T. Oyama, Synthesis, characterization, and hydrotreating activity of several iron group transition metal phosphides, J. Catal., 208 (2002) 321-331.
[29] A. Wang, L. Ruan, Y. Teng, X. Li, M. Lu, J. Ren, Y. Wang, Y. Hu, Hydrodesulfurization of dibenzothiophene over siliceous MCM-41-supported nickel phosphide catalysts, J. Catal., 229 (2005) 314-321.
[30] L. Wang, Y. Weng, X. Wang, H. Yin, F. Wang, X. Xue, X. Liu, F. Wang, P. Duan, Y. Zhang, Synergistic bimetallic RuMo catalysts for selective rearrangement of furfural to cyclopentanol in aqueous phase, Catal. Commun., (2019) 105745.
[31] M. Tamura, N. Yuasa, Y. Nakagawa, K. Tomishige, Selective hydrogenation of nitroarenes to aminoarenes using a MoOx-modified Ru/SiO2 catalyst under mild conditions, Chem. Commun., 53 (2017) 3377-3380.
[32] P.A. Clark, S.T. Oyama, Alumina-supported molybdenum phosphide hydroprocessing catalysts, J. Catal., 218 (2003) 78-87.
[33] R. Cheng, Y. Shu, L. Li, M. Zheng, X. Wang, A. Wang, T. Zhang, Synthesis and characterization of high surface area molybdenum phosphide, Appl. Catal. A, 316 (2007) 160-168.
[34] M.I. Zaki, M.A. Hasan, F.A. Al-Sagheer, L. Pasupulety, In situ FTIR spectra of pyridine adsorbed on SiO2-Al2O3, TiO2, ZrO2 and CeO2: general considerations for the identification of acid sites on surfaces of finely divided metal oxides, Colloid Surf., A, 190 (2001) 261-274.
[35] Y.K. Lee, S.T. Oyama, Bifunctional nature of a SiO2-supported Ni2P catalyst for hydrotreating: EXAFS and FTIR studies, J. Catal., 239 (2006) 376-389.
[36] P. Liu, Y.-L. Zhu, L. Zhou, W.-H. Zhang, Y.-X. Li, Amorphous Nickel Phosphide Nanoparticles for Selective Hydrogenation of Cinnamaldehyde, Catal. Lett., (2020).
[37] J. Xu, T. Liu, J. Li, B. Li, Y. Liu, B. Zhang, D. Xiong, I. Amorim, W. Li, L. Liu, Boosting the hydrogen evolution performance of ruthenium clusters through synergistic coupling with cobalt phosphide, Energ Environ Sci, 11 (2018) 1819-1827.
[38] J.X. Chen, Y. Yang, H. Shi, M.F. Li, Y. Chu, Z.Y. Pan, X.B. Yu, Regulating product distribution in deoxygenation of methyl laurate on silica-supported Ni-Mo phosphides: Effect of Ni/Mo ratio, Fuel, 129 (2014) 1-10.
[39] J.A. Rodriguez, J.Y. Kim, J.C. Hanson, S.J. Sawhill, M.E. Bussell, Physical and chemical properties of MoP, Ni2P, and MoNiP hydrodesulfurization catalysts: Time-resolved X-ray diffraction, density functional, and hydrodesulfurization activity studies, J. Phys. Chem. B, 107 (2003) 6276-6285.

[40] R. Gao, L. Pan, H. Wang, Y. Yao, X. Zhang, L. Wang, J.-J. Zou, Breaking trade-off between selectivity and activity of nickel-based hydrogenation catalysts by tuning both steric effect and d-band center, Advanced Science, 6 (2019) 1900054.
[41] Y. Li, H. Cheng, W. Lin, C. Zhang, Q. Wu, F. Zhao, M. Arai, Solvent effects on heterogeneous catalysis in the selective hydrogenation of cinnamaldehyde over a conventional Pd/C catalyst, Catalysis Science & Technology, 8 (2018) 3580-3589.
[42] X. Lan, K. Xue, T. Wang, Combined synergetic and steric effects for highly selective hydrogenation of unsaturated aldehyde, J. Catal., 372 (2019) 49-60.
[43] V. Ponec, On the role of promoters in hydrogenations on metals; α,β-unsaturated aldehydes and ketones, Appl. Catal. A, 149 (1997) 27-48.
[44] N.R. Avery, W.H. Weinberg, A.B. Anton, B.H. Toby, End-On and Side-On Bonding of Ketones to Surfaces: Acetone on the Ru(001) and Pt(111) Surfaces, Phys. Rev. Lett., 51 (1983) 682-685.
[45] R.D. Srivastava, A.K. Guha, Kinetics and mechanism of deactivation of Pd□Al2O3 catalyst in the gaseous phase decarbonylation of furfural, J. Catal., 91 (1985) 254-262.
[46] S. Nishiyama, T. Hara, S. Tsuruya, M. Masai, Infrared Spectroscopy Study of Aldehydes Adsorbed on Rh−Sn Bimetallic Systems: Selective Activation of Aldehydes by Tin, J. Phys. Chem. B, 103 (1999) 4431-4439.
[47] F. Delbecq, P. Sautet, Competitive C□C and C□O Adsorption of α-β-Unsaturated Aldehydes on Pt and Pd Surfaces in Relation with the Selectivity of Hydrogenation Reactions: A Theoretical Approach, J. Catal., 152 (1995) 217-236.
[48] S.F. Shafna, K.S. Resmi, M.Y. Sheena, C.Y. Panicker, B. Harikumar, FT-IR, FT-Raman, NLO, MEP, NBP and molecular docking study of 2-phenyl-1-propanol, Science Letters Journal, 4 (2015).
[49] K. Momma, F. Izumi, VESTA 3 for three-dimensional visualization of crystal, volumetric and morphology data, J. Appl. Crystallogr., 44 (2011) 1272-1276.
[50] W. Humphrey, A. Dalke, K. Schulten, VMD: Visual molecular dynamics, J. Mol. Graph., 14 (1996) 33-38.